Design and Optimization of an Integrated Resonant Inductor With High-Frequency Transformer for Wide Gain Range DC–DC Resonant Converters in Electric Vehicle Charging Applications

Satyaki Mukherjee, *Member, IEEE*, and Peter Barbosa, *Senior Member, IEEE*

***Abstract*—Large-scale adoption of wide band gap semiconductors in switched-mode power converters enables miniaturization of power electronic systems. With switching frequencies approaching a few hundred kilohertz–megahertz range, efficient and compact design of magnetic components are crucial for future generation power supplies in data centers or electric vehicle (EV) applications. In a typical two-stage AC–DC power supply, the DC–DC stage is often constructed using a resonant converter with galvanic isolation provided by a high-frequency transformer. In such systems, the integration of an inductor in the resonant network with the transformer helps improve power density and reduces component count and cost. However, the integration of magnetic components can result in increased losses, deteriorating the performance of the power conversion system. In this article, a magnetic structure along with an optimization methodology is presented to integrate a predefined resonant inductor as leakage inductance of the high-frequency transformer achieving minimum penalty on converter efficiency using planar core geometry and printed circuit board (PCB)-based windings. The proposed methodology is applied to integrate a 7.8 μH inductor with a 2:1 transformer for a 6.6-kW, 500-kHz LCL-T resonant DC–DC stage utilizing gallium nitride transistors in an onboard battery charging converter. On the prototype converter using the optimized integrated magnetic component, a peak efficiency of 98.4% was obtained using PCB windings. Furthermore, the integrated magnetic component achieved 64-kW/L power density in the demonstrator prototype.**

***Index Terms*—AC losses, electric vehicle (EV) chargers, high-frequency magnetics, magnetic integration, planar magnetics using PCB windings, programmable leakage inductance, resonant converters.**

I. Introduction

TO KEEP up with the increasing demand for higher power densities in high-efficiency power electronic converters, the design and optimization of high-frequency magnetic components (including both inductors and isolation transformers) have gained widespread attention in the telecommunication, automotive, data center, renewable energy storage and, aerospace industries. Although it is well understood that elevated switching frequencies reduce the energy storage requirement on magnetic components, the size of an appropriate magnetic component, however, is a more involved question. To appropriately size magnetic components variety of considerations regarding winding losses [1], [2], [3], permeability of magnetic materials and core losses [4], [5] along with thermal and heat transfer limits [6], [7], [8] need to be considered. Furthermore, the labor-intense manufacturing complexity associated with conventional Litz wire and copper foil-based windings obstructs the automation and repeatability of power electronic systems [9]. With the rapid growth in printed circuit board (PCB) technology, features of low-profile planar magnetic components such as higher power density, superior thermal performance, unrivaled repeatability and modularity, ease of manufacturing, and predictable parasitics have gained a lot of popularity [10], [11], [12], [13]. Another consideration to this end is the rapid proliferation of wide bandgap semiconductors such as gallium nitride (GaN) and silicon carbide, enabling high-frequency switching. At switching frequencies of several hundred kilohertz to megahertz, not only the core size of magnetic components can be reduced but also the number of turns in both inductors and transformers can be tapered off, enabling the use of 6–10 layer heavy copper PCBs, which alternatively suffers from higher costs and lower fill factors at lower frequencies [13], [14]. Additionally, many popular high-power isolated DC–DC converter topologies require an inductor in series with the isolation transformer [15], and integration of this series inductance as a programmable leakage of the isolation transformer further lowers the cost and increases the power density of such converters [16]. Attempts of increased spacing between primary and secondary windings in the core window to generate additional leakage inductance do not lend themselves well in generating well-defined leakage inductance and also reduce core utilization, as the leakage flux is contained in the air [17]. In the existing literature, there are alternate approaches illustrating the integration of a programmable inductor with the isolation transformer using custom core structures [18],

Manuscript received 11 November 2022; revised 22 December 2022; accepted 7 February 2023. Date of publication 10 February 2023; date of current version 10 March 2023. This work was supported by Delta Electronics (Americas). Recommended for publication by Associate Editor O. Lucia. *(Corresponding author: Satyaki Mukherjee.)*

The authors are with the Milan M. Jovanović Power Electronics Laboratory (MPEL), Delta Electronics (Americas), Ltd., Durham, NC 27709 USA (e-mail: satyaki.mukherjee@colorado.edu; peter.barbosa@deltaww.com).

Color versions of one or more figures in this article are available at https://doi.org/10.1109/TPEL.2023.3243807.

Digital Object Identifier 10.1109/TPEL.2023.3243807

[19], [20], insertion of magnetic shunts [21], [22] or by the distribution of windings around outer posts of the core [9], where the leakage flux is controlled and guided by the use of a magnetic core.

In all the existing integration approaches, a clear tradeoff between manufacturing complexity, power density, and the efficiency of the component has been demonstrated. To facilitate the generation of programmable leakage inductance, perfect interleaving between the primary and secondary of a transformer needs to be disrupted, which subsequently results in larger AC winding losses [1], [23]. Whereas, if the interleaving is kept intact to a large degree, the core suffers from increased AC flux density originating from the leakage flux and associated hysteresis and eddy current losses. The magnetic structure proposed in [9] and [16] utilizes asymmetrical distribution of primary and secondary turns around the two outer posts and an airgap on the center post of an "E" shaped core segment to control the leakage inductance.

Due to the flexibility of routing in PCB-based winding implementation, this solution is very attractive for high-frequency planar magnetic designs with PCB-embedded windings. This strategy has two degrees of freedom to design and control the leakage inductance, which results in completely different tradeoffs from winding and core loss perspectives. The tradeoffs associated with such designs are yet to be explored in the prior works published in the literature. Hence, this work focuses on the "E+I" core-based asymmetrically distributed winding structure and finds the optimal way of generating the desired leakage inductance. The key contributions of this article can be summarized as follows.

1) Establish a general solution for an "E+I" core-based integrated magnetic structure with programmable leakage inductance. This solution captures a large design space capable of meeting the same specifications and provides insights into a potential optimization of the component for minimum loss.
2) Analyze the impact of the interaction between magnetizing and leakage flux in the proposed component for "E+I" geometry and accommodate appropriate modifications to sustain this interaction without increasing the area and volume of the component.
3) Optimize the core geometry and the distribution of primary and secondary turns around the two outer posts of the "E" segment to arrive at the best tradeoff between core and winding losses.

The rest of this article is organized as follows: Section II introduces the integrated magnetic component and points to the major loss mechanisms in separate implementations of a transformer and a resonant inductor along with the losses associated with an integrated implementation. Key equations determining flux density in separate magnetic components are revisited to draw parallels with the integrated magnetic component. Section III provides a reluctance-model-based derivation of the major quantities in the integrated component along with an intuitive understanding of the programmable leakage inductance generation. Next, Section IV provides an overview of a particular application example, where a wide gain range DC–DC resonant converter for electric vehicle (EV) battery charging is illustrated as a use case of the integrated magnetic component. Following this, the optimization of the integrated magnetic structure for this particular application example is provided. Experimental results on a prototype converter utilizing the optimized integrated magnetic component are presented in Section V. Finally, Section VI summarizes the findings in the article and concludes.

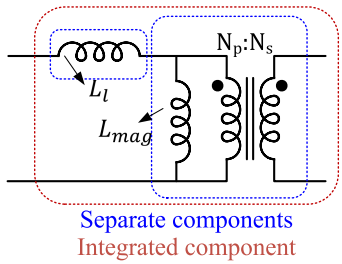

Fig. 1. Example two port magnetic component integrating a transformer with $N_p : N_s$ turns ratio and a resonant inductor L_l. Transformer's magnetizing inductance L_{mag} and leakage inductance are lumped at the primary side.

II. Overview of Major Loss Mechanisms and Description of Integrated Magnetic Component

Fig. 1 shows a circuit configuration very common to many isolated DC–DC converters, where an inductor L_l is placed in series with a transformer having turns ratio of $N_p : N_s$. Generally, the value of the inductor L_l is a design parameter for the DC–DC converter and determines several tradeoffs associated with its operation and performance. However, the leakage inductance of the transformer in traditional designs is difficult to control. Moreover, to reduce proximity effect-related losses in the transformer, generally primary and secondary windings are interleaved, which further reduces the leakage inductance of the transformer.

Compared to Litz-wire-based magnetic components, PCB windings additionally suffer from increased high-frequency AC winding losses due to the limitations in copper thickness and their inability to twist like Litz wires to reduce proximity effect-related winding losses. Fig. 2(a) shows an example PCB winding-based inductor with planar E and I cores. The inductance of this component can be adjusted using the airgap between the E and I core segments along with the number of turns. However, as there is no interleaving possible, the proximity losses in this component can be usually very high, as the number of winding layers increases, which can be modeled using Dowell's equation for rectangular conductors [1], [24], [25]

$$F_R = \frac{R_{\text{ac}}}{R_{\text{dc}}} = \phi\left((2\,m^2 - 2m + 1)\frac{\sinh(2\phi) + \sin(2\phi)}{\cosh(2\phi) - \cos(2\phi)} - 4m(m-1)\frac{\sinh(\phi)\cos(\phi) + \cosh(\phi)\sin(\phi)}{\cosh(2\phi) - \cos(2\phi)}\right) \quad (1)$$

where $\phi = h/\delta$ indicates the effective winding depth obtained by dividing the actual conductor thickness h, with skin depth at the operating frequency $\delta = \sqrt{\rho/\pi\mu f}$ and m denotes the layer number. Furthermore, due to the low profile of the core, the top winding layer does not only suffer from proximity losses from the nearby windings but also due to the proximity of the air gap.

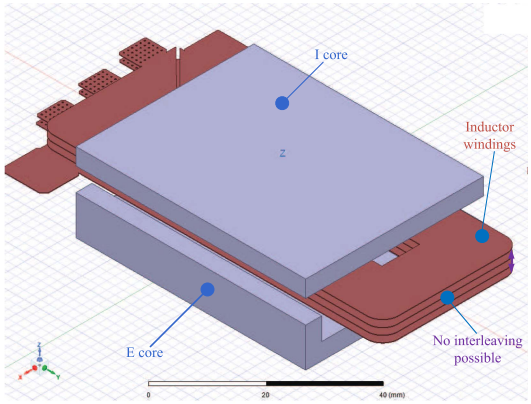

(a)

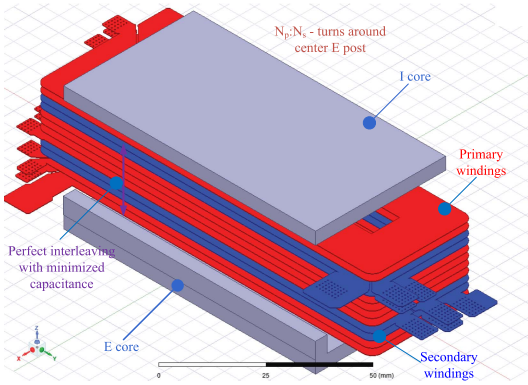

(b)

Fig. 2. Example of separately optimized planar magnetic components utilizing standard E+I cores. (a) 4-turn planar inductor with airgap where no interleaving is possible. (b) 8:4 fully interleaved planar transformer, where all the windings are around the center post of the E core.

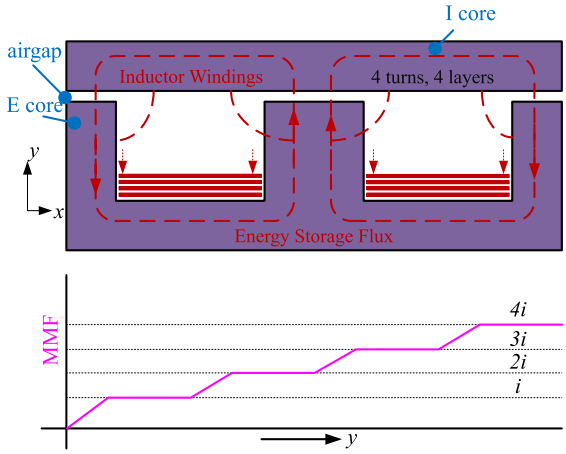

(a)

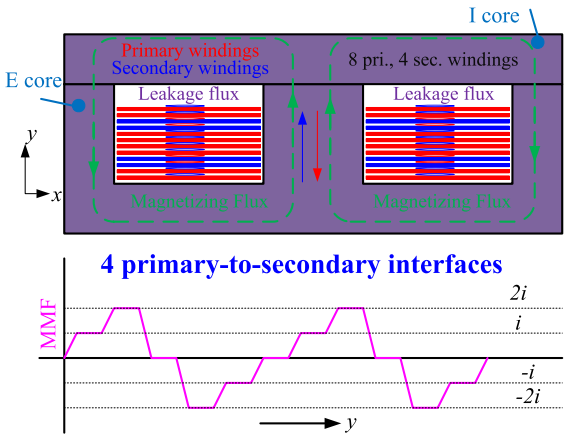

(b)

Fig. 3. Two-dimensional cross-sectional view for the planar magnetic components described in Fig. 2. (a) For the 4-turn noninterleaved airgapped inductor, along y dimension of the core window, MMF increases linearly causing proximity losses. (b) For the 8:4 perfectly interleaved transformer, MMF in the core window never increases beyond $2i$ causing very little proximity effect and leakage inductance. Fluxes passing through the ferrite core for the transformer fully couple both primary and secondary windings, resulting in very little leakage flux circulating through air.

The presence of increased H-fields due to the combined effect of the nearby conductors and fringing fields from airgap [26] makes the design of a separate inductor with PCB windings challenging. From (1), it is imperative that increasing number of layers to accommodate a lower surface area will result in very high proximity losses for a separate inductor without any interleaving even with a small skin depth ϕ. In Fig. 3(a), the MMF diagram along the height of a planar magnetic inductor with PCB windings is shown. It can be seen how, due to lack of interleaving, the top winding layer sees increased MMF, resulting in larger winding losses. On the other hand, generally, the core losses in AC inductors are proportional to the peak of AC flux density

$$B_{\text{ac,pk}} = \frac{L i_{\text{ac,pk}}}{N A_e} \tag{2}$$

where L is the inductance, $i_{\text{ac,pk}}$ is the peak of the AC current flowing through the inductor, N is the number of turns in the inductor, and A_e is the core's cross-sectional area. It should be noted that for an inductor, the flux density in the core is directly proportional to the current flowing through the component. Next, a fully interleaved transformer is considered in Fig. 2(b) and the corresponding 2-D cross section along with the relevant MMF diagram is shown in Fig. 3(b). It should be observed that in comparison to the inductor shown in Fig. 3(a), the transformer MMF does not keep on increasing among the winding layers as the number of layers increase and can be reset using interleaved primary and secondary windings. Also, if transformers are designed with large magnetizing inductance and without any airgap, the fringing fields are absent in them, making the windings immune to proximity and fringing losses. Core losses in transformers are generally governed by applied volt–seconds on the windings, with the peak flux density expression given as

$$B_{\text{max}} = \frac{\int_0^{T_s/2} v_s(t)dt}{N_s A_e} \tag{3}$$

where $v_s(t)$ is the instantaneous secondary winding voltage, N_s is the number of secondary turns, and A_e is the area of

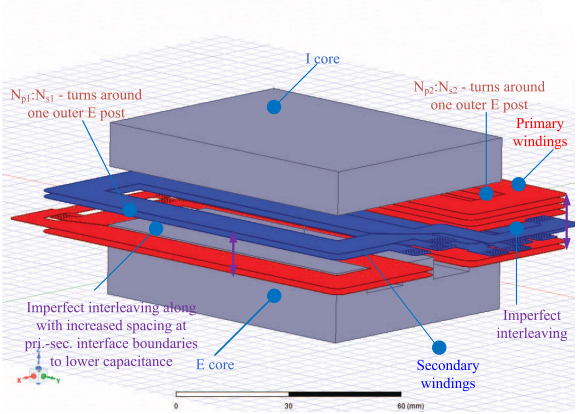

Fig. 4. Example three-dimensional view of the proposed integrated magnetic component using planar E+I core. It should be noticed that, in contrary to Figs. 2 and 3, the primary and secondary windings of transformer are placed around the outer posts of E core segment. Also, the total primary turns N_p and secondary turns N_s are distributed on the outer posts, resulting in two elemental transformers of turns ratio $N_{p1} : N_{s1}$ and $N_{p2} : N_{s2}$. These elemental transformers cannot maintain perfect interleaving, thus originating controllable leakage inductance with leakage flux flowing through the ferrite core.

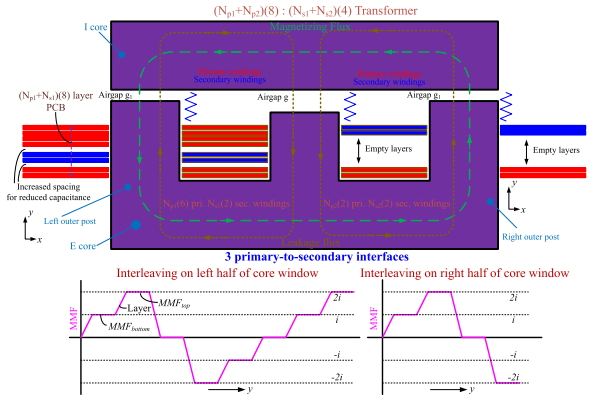

Fig. 5. Cross-sectional view of the proposed integrated magnetic component, where the total turns ratio between primary and secondary windings is kept as the original transformer. The customized height of the center post creates a different airgap g between the center post and I core segment compared to the airgap g_1 adjacent to the outer posts. These two airgaps along with the imperfect interleaving of windings illustrated by the MMF diagrams create controllable leakage and magnetizing inductance for this magnetic structure.

cross section of the center leg. Hence, unlike inductors (2), transformers can carry large winding currents without incurring core losses as long as the applied volt–seconds can be controlled using the $N_s A_e$ product. The winding losses in transformers, due to perfect interleaving and no airgap, are primarily determined by the DC resistance of the primary and secondary turns. From (3), it can be deduced that having a larger number of turns for a given turns ratio will yield lower transformer core losses at the expense of larger DC winding losses. Generally, fully interleaved transformers result in reduced AC winding loss and reduced leakage flux through the air (due to its larger reluctance) as shown in Fig. 3(b) with uncontrollable and small leakage inductance. To circumvent the issues associated with larger winding losses in a separate inductor and unpredictably low leakage inductance of a fully interleaved transformer, an integrated magnetic structure is shown in Fig. 4. In this case, an original transformer with a turns ratio of $N_p : N_s$ is first split into two separate transformers with turns ratio of $N_{p1} : N_{s1}$ and $N_{p2} : N_{s2}$, where $N_p = N_{p1} + N_{p2}$ and $N_s = N_{s1} + N_{s2}$. These two separate or elemental transformers are wound around the outer posts of the "E" core as shown in Fig. 4 unlike around the center post of a traditional transformer shown in Fig. 2(b). Now, by series connection of the primary and secondary turns of the two elemental transformers (consequently forcing the currents through the elemental transformers to be the same) and adding a controllable airgap on the center post, desirable leakage inductance can be created using only the transformer windings [9]. This approach eliminates a separate magnetic component and reduces component count in the converter and can result in increased power density.

Fig. 5 shows the cross-sectional view of the proposed magnetic component along with two distinct MMF diagrams associated with the two elemental transformers along the outer posts of the "E" core. It should be noted that the center post is now used as the leakage flux path, whereas the two outer

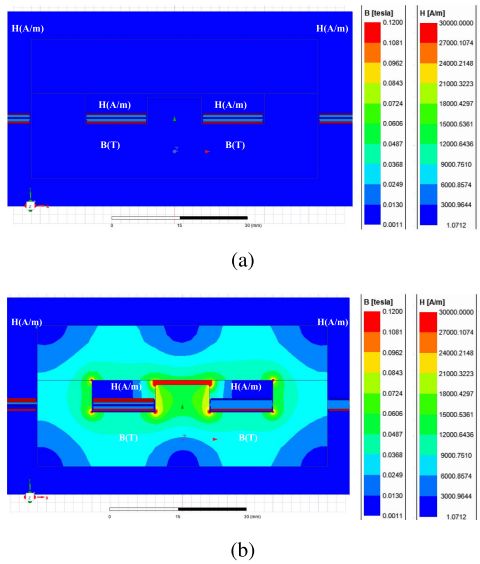

Fig. 6. Importance of asymmetrical distribution for primary and secondary turns in generating leakage inductance shown using 2-D FE simulations: (a) With symmetrical distribution of turns ($N_{p1} = 4, N_{s1} = 2, N_{p2} = 4, N_{s2} = 2$), although perfect interleaving can be maintained no leakage flux is established. Whereas (b) using the same magnetic core and airgap lengths, leakage flux is established with asymmetrical distribution of the turns ($N_{p1} = 6, N_{s1} = 2, N_{p2} = 2, N_{s2} = 2$). Excitation used in both simulations: $\hat{I}_p = 22\angle 0, \hat{I}_s = 44\angle 0$.

posts are carrying the magnetizing flux linking all the primary and secondary windings. Most importantly, the distribution of turns among the two outer E core posts cannot be equal to generate leakage inductance even with an airgap in the center post. Thus, the perfect interleaving achievable in a traditional transformer [see Fig. 2(b)] is broken in an integrated component, as they still are forced to carry the same winding currents. To illustrate the effect of turns distribution and airgap on the center post, Fig. 6 shows a 2-D finite element (FE) simulation of

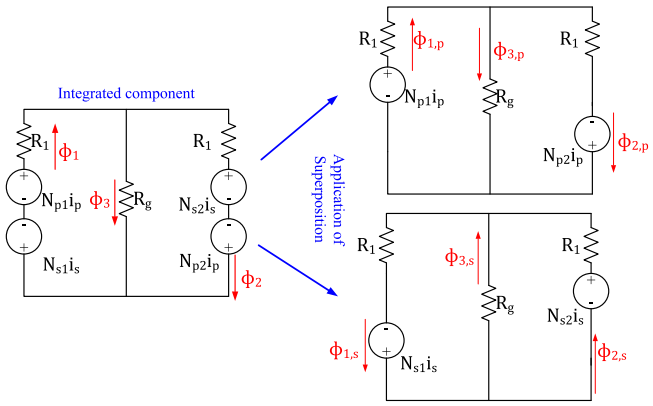

Fig. 7. Reluctance of the proposed magnetic component shown in Fig. 4, comprising of two elemental transformers around the outer posts of "E" core segment. This reluctance model can be solved using the superposition theorem, to find out self and mutual inductances of primary and secondary windings.

the proposed magnetic structure with two different designs. In Fig. 6(a), turns N_p and N_s of the original transformer are equally distributed between the outer posts. In this case, when an ideal transformer excitation is used without any magnetizing current (i.e., $i_p = \frac{N_s}{N_p} i_s$), no leakage flux is obtained even with an airgap on the center post as all the flux flows through the outer posts linking both coils. In Fig. 6(b), when the symmetry is broken in the turns distribution of the elemental transformers, the leakage flux path is visible. Hence, it is obvious that to generate leakage inductance, the distribution of the turns needs to be asymmetrical, which will result in loss of interleaving as indicated by an example MMF diagram of the proposed magnetic structure shown in Fig. 5. As interleaving is disrupted, the magnetic component is capable of generating leakage flux and consequently leakage inductance but suffers from proximity effect-related AC winding losses as discussed earlier. To draw more insights into the tradeoffs in an integrated design, a general study of the magnetic structure shown in Fig. 4 is developed in the following section.

III. General Solution of Proposed Integrated Magnetic Component

In this section, first, a general analysis of the integrated magnetic structure is presented using a standard reluctance model of the geometry shown in Fig. 5 with an application of the superposition theorem. This general analysis helps in understanding the tradeoffs associated with different possible designs for the same specifications of the integrated component. Next, an intuitive understanding of the interaction between the leakage and magnetizing flux of the component is discussed.

A. Reluctance Modeling

The total reluctance model of the integrated component is shown in Fig. 7, comprising four magneto motive force (MMF) sources corresponding to N_{p1}, N_{s1}, N_{p2}, and N_{s2} windings and 3 reluctances of the E core posts. The reluctances can be solved from the airgaps shown in Fig. 5 as

$$R_1 = \frac{l_{g1}}{\mu_0 A_e}; R_g = \frac{l_g}{\mu_0 A_e}. \tag{4}$$

To find out the self and mutual inductance of the elemental transformers, the flux linkages associated with the windings need to be obtained first. Hence, the reluctance model needs to be analyzed using the superposition theorem. First, when only the primary windings are excited, the flux in the three core legs of the E core can be solved as

$$\begin{aligned}\phi_{1,p} &= \frac{i_p\left((N_{p1}+N_{p2})R_g + N_{p1}R_1\right)}{2R_1R_g + R_1^2}\\ \phi_{2,p} &= \frac{i_p\left((N_{p1}+N_{p2})R_g + N_{p2}R_1\right)}{2R_1R_g + R_1^2}\\ \phi_{3,p} &= \frac{i_pR_1\left(N_{p1}-N_{p2}\right)}{2R_1R_g + R_1^2}.\end{aligned} \tag{5}$$

Then, the self $\lambda_{p,p}$ and mutual $\lambda_{p,s}$ flux linkages can be derived as

$$\lambda_{p,p} = N_{p1}\phi_{1,p} + N_{p2}\phi_{2,p}; \lambda_{p,s} = N_{s1}\phi_{1,p} + N_{s2}\phi_{2,p}. \tag{6}$$

Following which, by definition, the self and mutual inductances with primary windings excited can be solved as

$$\begin{aligned}L_{p,p} &= \frac{\lambda_{p,p}}{i_p} = \frac{(N_{p1}+N_{p2})^2R_g + (N_{p1}^2+N_{p2}^2)R_1}{2R_1R_g + R_1^2}\\ M_{p,s} &= \frac{\lambda_{p,s}}{i_p} = \frac{(R_g+R_1)(N_{s1}N_{p1}+N_{s2}N_{p2})}{2R_1R_g + R_1^2}\\ &\quad + \frac{R_g(N_{s1}N_{p2}+N_{s2}N_{p1})}{2R_1R_g + R_1^2}.\end{aligned} \tag{7}$$

From the self-inductance and mutual inductance shown in (7), the leakage inductance contributed by the primary windings, can be derived as

$$\begin{aligned}L_{l,p} &= L_{p,p} - M_{p,s}\frac{N_{p1}+N_{p2}}{N_{s1}+N_{s2}}\\ &= \frac{(N_{s2}N_{p1}-N_{s1}N_{p2})(N_{p1}-N_{p2})R_1}{(N_{s1}+N_{s2})(2R_1R_g + R_1^2)}.\end{aligned} \tag{8}$$

Similarly, when only the secondary coils are excited, from the second equivalent circuit in Fig. 7, first, the fluxes in the core legs can be calculated as

$$\begin{aligned}\phi_{1,s} &= \frac{i_s\left((N_{s1}+N_{s2})R_g + N_{s1}R_1\right)}{2R_1R_g + R_1^2}\\ \phi_{2,s} &= \frac{i_s\left((N_{s1}+N_{s2})R_g + N_{s2}R_1\right)}{2R_1R_g + R_1^2}\\ \phi_{3,s} &= \frac{i_sR_1\left(N_{s1}-N_{s2}\right)}{2R_1R_g + R_1^2}\end{aligned} \tag{9}$$

following which, the self and mutual inductances seen from the secondary windings can be solved in a similar way as

shown in (7)

$$\begin{aligned} L_{s,s} &= \frac{N_{s1}\phi_{1,s} + N_{s2}\phi_{2,s}}{i_s} \\ &= \frac{(N_{s1}+N_{s2})^2 R_g + (N_{s1}^2 + N_{s2}^2)R_1}{2R_1R_g + R_1^2} \\ M_{s,p} &= \frac{N_{p1}\phi_{1,s} + N_{p2}\phi_{2,s}}{i_s} \\ &= \frac{(R_g+R_1)(N_{s1}N_{p1} + N_{s2}N_{p2})}{2R_1R_g + R_1^2} \\ &\quad + \frac{R_g(N_{s1}N_{p2} + N_{s2}N_{p1})}{2R_1R_g + R_1^2}. \end{aligned} \tag{10}$$

Finally, the leakage inductance contributed by the secondary windings can be derived from (10) as

$$\begin{aligned} L_{l,s} &= L_{s,s} - M_{s,p}\frac{N_{s1}+N_{s2}}{N_{p1}+N_{p2}} \\ &= \frac{(N_{p2}N_{s1} - N_{p1}N_{s2})(N_{s1}-N_{s2})R_1}{(N_{p1}+N_{p2})(2R_1R_g + R_1^2)}. \end{aligned} \tag{11}$$

From (8) and (11), it is easy to observe that if the primary and secondary windings are equally distributed around the outer posts, making $N_{p1} = N_{p2}$ or, $N_{s1} = N_{s2}$, the corresponding winding will not contribute to any leakage inductance. It is also important to note that since the leakage flux is flowing through the gapped center post (unlike a traditional fully interleaved transformer—where the leakage flux flows through the air), the leakage inductance is much more well-controlled and predictable using the first-order reluctance model. The total leakage inductance seen from the primary side of the transformer (in accordance to the equivalent circuit shown in Fig. 1) can then be obtained from (8) and (11) as

$$L_l = L_{l,p} + \frac{(N_{p1}+N_{p2})^2}{(N_{s1}+N_{s2})^2}L_{l,s} = \frac{2(N_{s2}N_{p1} - N_{p2}N_{s1})^2}{(2R_g+R_1)(N_{s1}+N_{s2})^2}. \tag{12}$$

A few key observations can be made from (12). First, when $R_g \gg R_1$, the expression of total leakage inductance can be simplified to

$$L_l \approx \frac{\mu_0 A_e}{l_g}\frac{(N_{s2}N_{p1} - N_{s1}N_{p2})^2}{(N_{s1}+N_{s2})^2}. \tag{13}$$

From (13), it is easy to comprehend that the leakage inductance can be controlled either by the reluctance of the center post (by modifying the length of airgap: l_g, or area of cross section: A_e), or, it can also be controlled using the asymmetry in the number of turns distribution among the two outer posts. Upon closer inspection, it can be realized that $(N_{s2}N_{p1} - N_{s1}N_{p2})/(N_{s1}+N_{s2})$ behaves as an equivalent number of turns to realize the integrated leakage inductance. Hence, in this magnetic structure, if the asymmetry in winding distribution is increased—effectively providing more turns to generate the leakage inductance, interleaving is disrupted to a larger degree and winding losses increase, similar to the proximity effect in a separate inductor discussed in Section II. Whereas for the same desirable leakage inductance, the leakage flux density in the core reduces with larger asymmetry in turns distribution, resulting in lower core losses [following (2)]. The optimal distribution in the number of turns to minimize total losses will depend on the specifications of the component and will be further discussed using a design example in Section IV.

Although using the reluctance model in Fig. 7, (12) derives the total leakage inductance of the magnetic structure, it should be noted that the flux density in the core for such an integrated magnetic structure, does not only depend on the leakage flux but also depends on the magnetizing flux (as this single component carries both leakage and magnetizing flux). The magnetizing inductance referred to the primary or secondary side can be calculated from the mutual inductances found in (7) and (10) as (under the assumption that $R_g \gg R_1$)

$$L_{\text{mag,pri}} \approx \frac{(N_{p1}+N_{p2})^2}{2R_1}; L_{\text{mag,sec}} \approx \frac{(N_{s1}+N_{s2})^2}{2R_1}. \tag{14}$$

From (13) and (14), it is interesting to observe how the distribution of turns or the reluctance of the center post does not impact the magnetizing inductance. This can also be intuitively understood by the fact that the fluxes linking all the windings (magnetizing flux) are flowing only through the outer posts of the E core, making magnetizing inductance independently controllable by R_1. The magnetizing flux also complicates the flux distribution in the core. As the leakage flux is flowing through all parts of the core, but magnetizing flux is confined only in the base plates and the outer posts of the E core segment, the interaction of these two fluxes and their implication on losses deserves further attention. This topic is discussed in the following section.

B. *Impact of Magnetizing Flux on Core Geometry and Flux Density*

Standard "E" core constructions have a center post with twice larger cross-sectional area compared to the outer posts and base plates as shown in the separate components of Figs. 2 and 3 since the flux in the outer posts is halved compared to the center post. However, in the integrated magnetic component, as the fluxes do not originate from the center post, the interaction of magnetizing flux and leakage flux makes the flux distribution in the core different than the separate components. To understand this phenomenon, first, the fluxes ϕ_1, ϕ_2, and ϕ_3 can be solved using the superposition circuits obtained from the reluctance model in Fig. 7 as

$$\begin{aligned} \phi_1 &= \phi_{1,p} - \phi_{1,s} \\ &= \underbrace{-\frac{R_g}{2R_gR_1 + R_1^2}[(N_{s1}+N_{s2})i_s - (N_{p1}+N_{p2})i_p]}_{\text{magnetizing flux}} \\ &\quad + \underbrace{\frac{N_{p1}i_p - N_{s1}i_s}{2R_g + R_1}}_{\text{leakage flux}} \\ \phi_2 &= \phi_{2,p} - \phi_{2,s} \end{aligned}$$

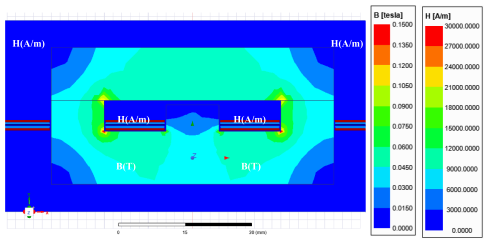

(a)

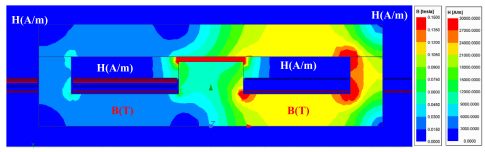

(b)

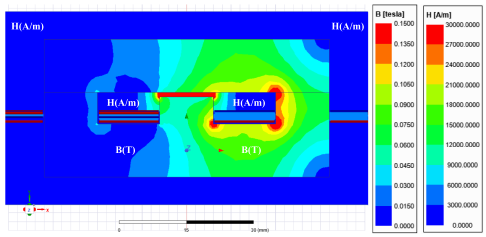

(c)

Fig. 8. To evaluate the impact of magnetizing flux, 3 distributed winding E+I core structures are simulated using the excitation of $\hat{I}_p = 22\angle 0, \hat{I}_s = 45.14\angle -0.5^\circ$. In (a), the windings are distributed symmetrically as Fig. 6(a); hence, no leakage flux is present in the center post of the E core and magnetizing flux only circulates through the outer posts. With asymmetrical windings similar to Fig. 6(b), when a standard E core shape is used with outer posts having half the area of cross section compared to the center post, the interaction between leakage and magnetizing flux is visible on the outer post. Finally, (c) shows the modified E core geometry with the same winding configuration as Fig. 6(b), where both leakage and magnetizing flux is present and their interaction does not result in very high flux density in any part of the core.

$$= \underbrace{-\frac{R_g}{2R_gR_1 + R_1^2}[(N_{s1} + N_{s2})i_s - (N_{p1} + N_{p2})i_p]}_{\text{magnetizing flux}} \underbrace{-\frac{N_{s2}i_s - N_{p2}i_p}{2R_g + R_1}}_{\text{leakage flux}}$$

$$\phi_3 = \phi_{3,p} - \phi_{3,s} = \underbrace{\frac{N_{p1}i_p - N_{s1}i_s + N_{s2}i_s - N_{p2}i_p}{2R_g + R_1}}_{\text{leakage flux}}. \tag{15}$$

From (15), it can be seen how the magnetizing flux component $R_g/(2R_gR_1 + R_1^2)[(N_{s1} + N_{s2})i_s - (N_{p1} + N_{p2})i_p]$ circulates between the outer posts and shows up in ϕ_1 and ϕ_2. This flux becomes zero, for an ideal transformer with infinite magnetizing inductance (when $(N_{p1} + N_{p2})i_p = (N_{s1} + N_{s2})i_s$). However, the leakage flux is distributed among all the posts. As illustrated in Fig. 5, in one of the outer posts and adjoining base plates the leakage flux and magnetizing flux adds up, whereas at the other outer post and adjoining base plates, the fluxes cancel each other. As the two fluxes are very different by nature [leakage being proportional to the transformer current (2), magnetization being proportional to applied volt–seconds (3)], the cancellation of fluxes can not be taken advantage of, but the addition of them requires a larger area of cross section to keep the flux-density within allowable limits further limiting core losses.

This interaction is visually illustrated using 2-D FEM simulations in Fig. 8, where unlike Fig. 6, the windings are excited with magnetizing current, thus making $(N_{p1} + N_{p2})i_p \neq (N_{s1} + N_{s2})i_s$. First, in Fig. 8(a), when the windings are equally distributed around the two outer posts, leakage flux becomes zero [similar to Fig. 6(a)] and the core only sees magnetizing flux circulating the outer pots and base plates. It should be noted, that the center post carries no flux in this case. In Fig. 8(b), when asymmetry is introduced, with a standard E core shape, it is visible that due to the addition of fluxes on the right outer post and adjacent base plates, the flux density becomes very high. Finally, in Fig. 8(c), the area of cross section for the outer posts and base plates is made equal to the center post enabling them to carry the unevenly distributed fluxes, which makes the component feasible by avoiding higher core losses under the same excitation as Fig. 8(b). The imbalance in flux density on the core posts is still visible, which will result in an uneven temperature rise of the core. After the thorough electromagnetic understanding of the integrated magnetic component developed in this section, the next section focuses on a particular application example of the component and provides design guidelines about how the turns should be distributed around the outer posts to get minimum loss in the component.

IV. Application Example of Proposed Magnetic Component

A. Overview of a Case-Study and Geometrical Parameter Optimization

Fig. 9 shows an isolated bidirectional resonant DC–dc converter utilized in onboard chargers for EVs [27]. Due to the availability of 800-V bus from a universal AC input 3-phase PFC stage, a stacked half-bridge inverter is utilized in the DC–DC converter enabling multilevel operation with 650-V GaN devices. Furthermore, a reconfigurable rectifier is used in either full-bridge or stacked half-bridge mode for better utilization of the rectifier devices while catering to 150–950 V battery voltage [27]. The resonant converter consists of LCL-T resonant network operating with fixed switching frequency [28]. This choice of resonant network is motivated for the wide gain range requirements of battery charging converters as illustrated by the charging profile shown in Fig. 10. More details about the benefits of this circuit can be found in [27]. The LCL-T resonant converter when designed to have the immittance characteristics acts like a constant voltage-to-current gain converter and makes constant current charging efficient [28], [29]. The constant power (CP) and constant voltage (CV) range of charging can be covered using a novel modulation scheme proposed in [27].

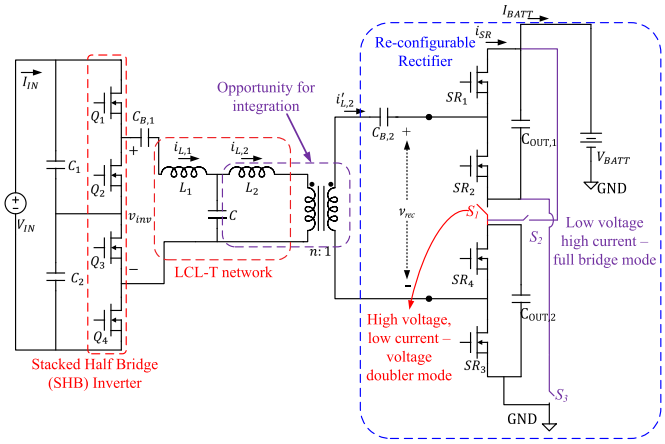

Fig. 9. Schematic diagram of an LCL-T resonant-network-based wide range isolated DC–DC converter operating from $V_{\text{IN}} = 800$ V with $V_{\text{BATT}} = 150 - 950$ V proposed in [27]. This converter operates with 650-V GaN devices at 500 kHz and features a resonant inductor L_2 connected in series with the isolation transformer. Thus, providing an opportunity to integrate these two components using the proposed magnetic structure of Fig. 4.

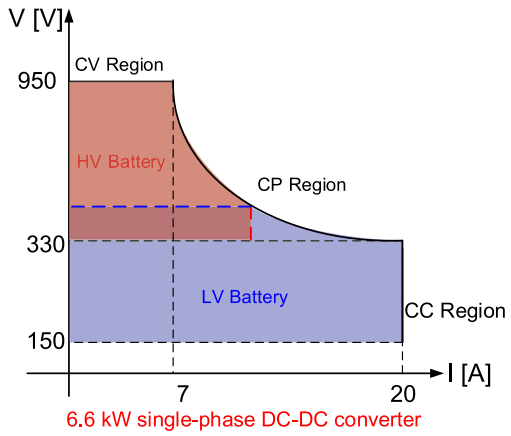

Fig. 10. Typical charging profile of a single phase DC–DC converter for EV charging applications encompassing entire voltage ranges of commercially available 400 and 800 V batteries.

This immittance design of the LCL-T network requires

$$L_1 = L_2 = L = \frac{X}{2\pi f_s}; C = \frac{1}{2\pi f_s X} = \frac{1}{4\pi^2 f_s^2 L}. \quad (16)$$

From Fig. 9, it can be seen that the inductance L_2 is a perfect candidate for integration with the transformer, and hence, the two separate components can be replaced using an integrated magnetic component, which is the focus of this article. As the LCL-T network achieves zero voltage switching (ZVS) using inductors L_1 and L_2, the transformer magnetizing current can be very small, making the magnetizing inductance L_m very big. To increase power density, a switching frequency of 500 kHz was selected, enabled by the superior switching performance of GaN devices. The design considerations of the passive components at 500 kHz for the charging profile of Fig. 10 are detailed in [27] and can be

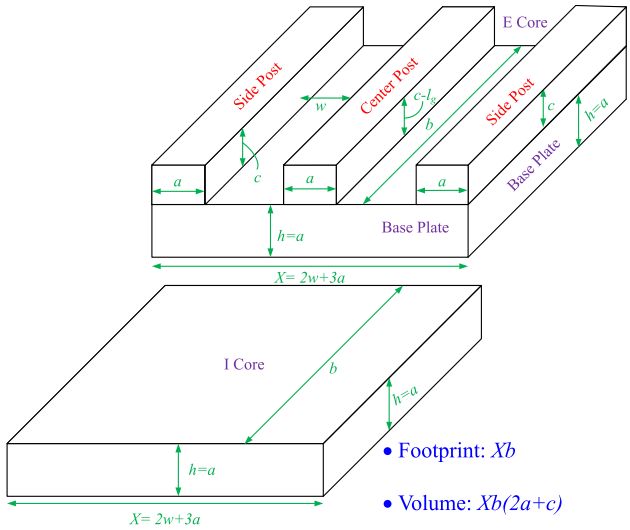

Fig. 11. Construction of the customized E+I core geometry prior to optimization of the distribution of turns around the two outer posts. The core dimensions are primarily determined from overall volume and footprint constraints along with conventional tradeoffs related to window area and area-off cross section for a given area-product $A_p = A_w A_e = (wc)(ab)$.

summarized as

$$N_p = 8; N_s = 4; X = 24.56\Omega; L_1 = L_2 = 7.8\mu\text{H}; C = 13\text{ nF}. \quad (17)$$

Hence, according to (17), the objective would be to design a 2:1 transformer [i.e., $(N_{p1} + N_{p2}) = 8; (N_{s1} + N_{s2}) = 4$] with 7.8 μH integrated leakage inductance. As a separate component-based design is presented in [27], which can be considered as a benchmark for the integrated design, and the proposed integrated magnetic component should have a similar total footprint and volume as the separate designs using standard EILP cores. In compliance with the low-profile nature of the converter and the impact of magnetizing and leakage flux interaction described in Section III-B, the core geometry of the magnetic component is shown in Fig. 11. It should be noted how the width of the outer posts and the thickness of the base plate is kept the same (with $h = a$) to have the same area of cross section in the flux path: $A_e = ab$. Furthermore, as the component footprint $(2w + 3a)b$ and the volume $(2w + 3a)(2a + c)b$ is given from the optimized separate design [27], a balanced tradeoff between winding DC resistance $R_{\text{dc}} \propto b/w$ and flux density $B_{\text{pk}} \propto 1/ab$ in the core should be considered to derive the optimal core dimensions. Core dimension c is also important to ensure a low profile of the component while having a sufficient height of the core to mitigate the fringing impact on the windings from the airgap on the center post. It should be noted that only b and w uniquely determine all other geometric parameters of the core once the footprint and volume are given

$$a = \frac{\frac{\text{Footprint}}{b} - 2w}{3}; c = \frac{\text{Volume}}{\text{Footprint}} - 2a. \quad (18)$$

The influence of the geometrical parameters of the core on losses is captured in Fig. 12, where for a given footprint of

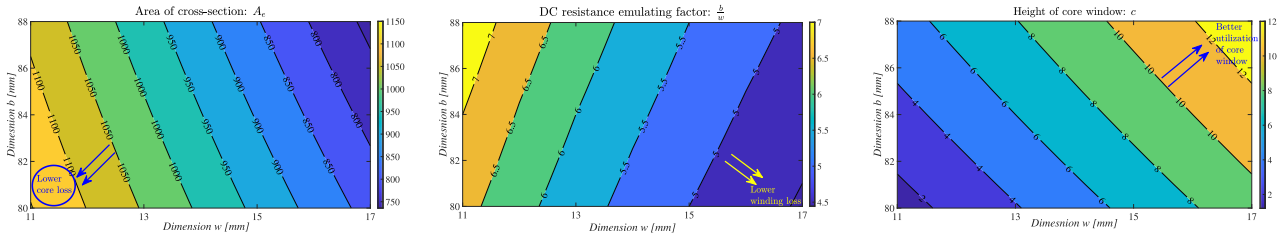

Fig. 12. Contour plots demonstrating the impact of core dimensions b and w for a given footprint of 5376 mm^2 and volume of 161 cm^3 on (a) core area of cross section A_e, (b) winding DC resistance and (c) window area utilization c.

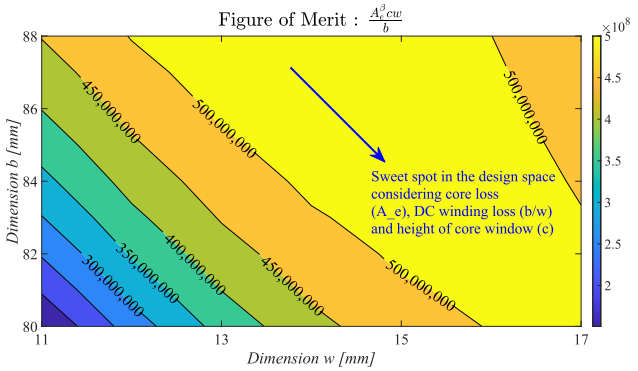

Fig. 13. Contour plot in the b, w plane of a figure-of-merit capturing all the dimensional impacts on core and winding losses, clearly demonstrating the sweet spot in the design space.

5376 mm^2 and volume of 161 cm^3, contour plots are shown for $A_e, b/w$, and c in the b versus w plane. In the contour plots, the contrasting impacts of core dimensions on core and winding losses can be identified. Minimizing core loss requires a smaller value of b and w, whereas to achieve better window utilization and lower winding resistance with minimized fringing impact, larger values of b and w are preferable, respectively. To uniquely optimize the core geometry, a figure of merit can be formulated capturing all the different loss mechanisms in the integrated magnetic component as

$$\text{Figure of Merit} = \frac{A_e^{\beta} cw}{b}. \tag{19}$$

Fig. 13 captures the impact of core dimensions on both kinds of losses using this figure of merit where β defines the core-loss coefficient of the particular ferrite core material used in the construction. Maximizing this factor would lead to minimizing total losses in the component. The contour plot in Fig. 13 leads to the identification of a sweet spot in the design plane, based on which the final core dimensions are picked as

$$a = 12 \text{ mm}; b = 84 \text{ mm}; c = 6 \text{ mm}; w = 14 \text{ mm}. \tag{20}$$

Next, considerations related to the distribution of turns and their impact on the loss are discussed while adhering to this particular core geometry.

B. Loss Modeling and Constrained Optimization Using Design Example

If the magnetizing inductance is sufficiently larger than the required leakage inductance then in Fig. 7 $R_g \gg R_1$, following which, from (13) and (14), it can be seen that the airgap in the center post along with the turns ratio distribution independently controls the leakage inductance. The magnetizing inductance can then be programmed by the reluctance of the outer posts along with total primary and secondary turns. Following this rationale, the total turn determination for primary and secondary windings follows the same optimization routine used routinely in literature based on magnetizing flux in a separate transformer with very small leakage inductance [11]. For leakage inductance optimization, if the magnetizing flux is ignored i.e., $(N_{p1} + N_{p2})i_p = (N_{s1} + N_{s2})i_s$, then from (15)

$$\phi_{3,lkg} = \frac{i_p \mu_0 A_e}{l_g} \frac{N_{s2}N_{p1} - N_{s1}N_{p2}}{N_{s1} + N_{s2}}; \phi_{1,\text{lkg}} = \phi_{2,\text{lkg}} = \frac{\phi_{3,\text{lkg}}}{2}. \tag{21}$$

Now, combining (13) and (21) results in

$$B_{3,lkg} = \frac{\phi_{3,lkg}}{A_e} = i_p \sqrt{\frac{\mu_0 L_l}{l_g A_e}}. \tag{22}$$

A very interesting conclusion can then be drawn from (13) and (22). For the same required leakage inductance in a given core geometry (A_e), if the asymmetry in turns distribution is reduced to get better interleaving and lesser proximity losses, the factor $N_{s2}N_{p1} - N_{s1}N_{p2} = (N_s - N_{s1})N_{p1} - (N_p - N_{p1})N_{s1} = N_sN_{p1} - N_pN_{s1}$ reduces. This will prompt a lower value of airgap l_g, which will make the leakage flux density increase (22). This intuitive tradeoff between higher asymmetry and lower flux density was discussed earlier, but (22) analytically confirms it. Hence, the obvious tradeoff between core and winding losses becomes clear to generate the same leakage inductance, which is not dependent on the total primary and secondary turns but solely dictated by the distribution of turns. This tradeoff is graphically illustrated using analytically obtained losses for all possible designs in Fig. 14, where the core geometry, magnetizing inductance, leakage inductance, and the total number of turns are kept constant but to obtain the required leakage inductance different combination of turns distribution and airgap length on the center post is used following the analytical expression in (13). First Fig. 14(a) shows how in

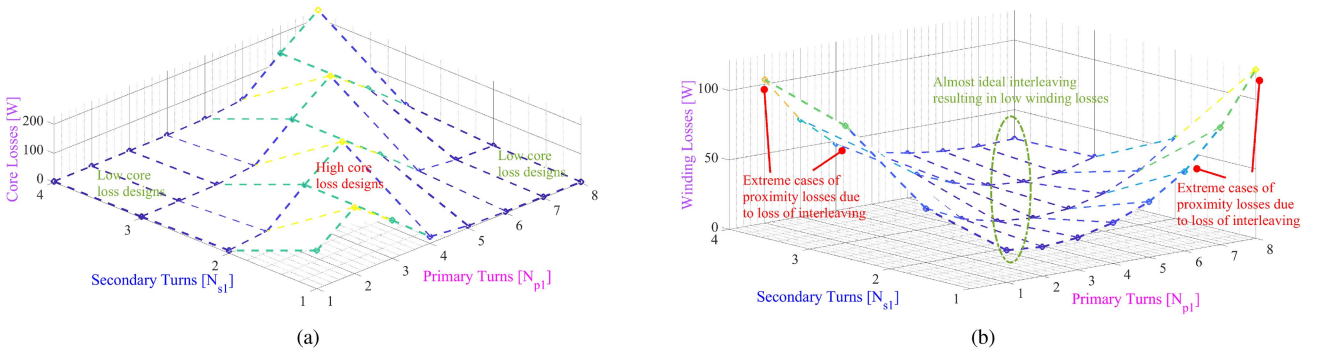

Fig. 14. 3-D mesh plots showing the tradeoffs associated with (a) core loss and (b) winding loss for a different distribution of windings around the outer posts of the E core segment. All the designs depicted in the diagrams maintain the same leakage inductance of $L_l = 7.8\,\mu$H and overall turns ratio of $N_p : N_s = 8:4$.

the N_{s1}, N_{p1} design space, core losses change. Here, core losses are obtained from the flux density expression obtained in (15), using Steinmetz parameters of DMEGC DMR 51-W material and application of improved Generalized Steinmetz Equation (iGSE) [4]. Since the fluxes in the core are purely AC in nature without any DC bias, the iGSE method yields accurate estimates for core losses. It should be observed how large asymmetrical designs result in very low core losses as airgap for such designs are relatively large and consequently leakage flux density is low (22). Hence, the core losses in such designs are solely contributed by the magnetizing flux. This trend is completely reversed in Fig. 14(b), where, in the same design space, AC winding losses are plotted using Dowell's equations [1] including the proximity effect-related losses discussed in Section II due to imperfect interleaving. For all possible designs in the space, the MMF on top and bottom of a certain layer can be first found depending on the degree of interleaving (as shown in Fig. 5). Then, the high-frequency winding losses in any particular layer (with one turn in one layer) can be found, based on the skin depth of the design (ϕ) as

$$P_{\text{layer}} = R_{\text{dc}}\phi\left[\left(\text{MMF}_{\text{top}}^2+\text{MMF}_{\text{bottom}}^2\right)\frac{\sinh(2\phi)+\sin(2\phi)}{\cosh(2\phi)-\cos(2\phi)} - 4\text{MMF}_{\text{top}}\text{MMF}_{\text{bottom}}\frac{\sinh(\phi)\cos(\phi)+\cosh(\phi)\sin(\phi)}{\cosh(2\phi)-\cos(2\phi)}\right] \tag{23}$$

where MMF_{top} and $\text{MMF}_{\text{bottom}}$ are the MMFs on the top and bottom of that particular layer. It can be seen from (23) that with larger asymmetry, interleaving is compromised to a larger degree (increasing MMF_{top} and $\text{MMF}_{\text{bottom}}$), resulting in higher winding losses in the layers. Finally, Fig. 15 shows the total loss in the same design space, where the optimal turns distribution can be identified as the points having a balanced tradeoff between core and winding losses. For minimum total loss operation, a design of $N_{p1} = 2, N_{s1} = 2, N_{p2} = 6, N_{s2} = 2$ is chosen in this particular design example. It should be noted that with a larger value of N_p and N_s, the design space grows and the impact of the optimization is more pronounced. An arbitrarily chosen asymmetric design can result in significantly higher loss compared to an optimal design.

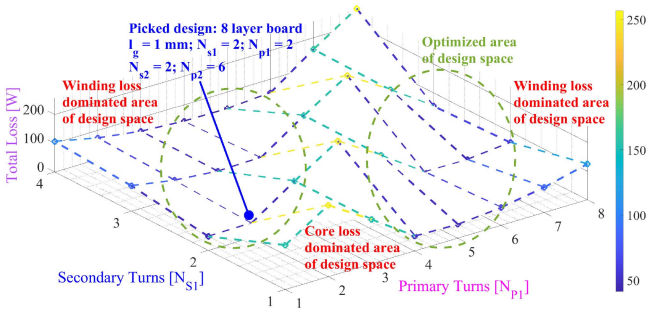

Fig. 15. 3-D mesh plot illustrating the minimization of total loss in the design space of N_{p1} and N_{s1}. The individual trends of core and winding losses shown in Fig. 14 are combined in the total loss. The final design is chosen according to practical design considerations as well as using the global minima in the design space.

The entire optimization process, from selecting the core dimensions to optimally picking the distribution of primary and secondary turns around the two outer posts of the "E" core is summarized in Fig. 16. To validate the analytical optimization process and gather more accurate winding loss estimations including the fringing effect from the airgap, the optimized final design is simulated using the Ansys Maxwell 3-D FE analysis. The simulation result is shown in Fig. 17. The impact of magnetizing flux and leakage flux interaction is visible in the flux density distribution of the core. Furthermore, the impact of current crowding near the airgap of the center post due to the fringing effect is also visible from the current density distribution. The inductance matrix obtained from the simulation is given as

$$\begin{bmatrix} v_1 \\ v_2 \end{bmatrix} = \begin{bmatrix} 694.25 & 343.73 \\ 343.73 & 172.01 \end{bmatrix} \mu\text{H}\frac{d}{dt}\begin{bmatrix} i_1 \\ i_2 \end{bmatrix}. \tag{24}$$

Which corresponds to a leakage inductance of

$$L_l = L_{11} - 2nL_{12} - n^2L_{22} = 7.37\,\mu\text{H}. \tag{25}$$

Similar to the inductance matrix in (24), the resistance matrix was also extracted from Ansys 3-D simulation for winding loss estimations [23]. As the simulation results matched the theoretical predictions fairly well an experimental prototype was

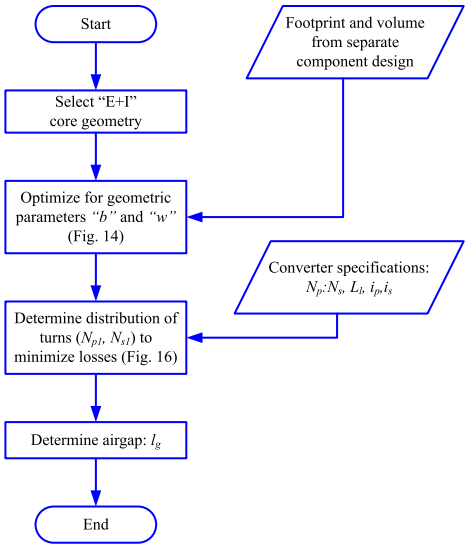

Fig. 16. Flowchart demonstrating step-by-step optimization process of the integrated magnetic component from given converter specifications and size constraints.

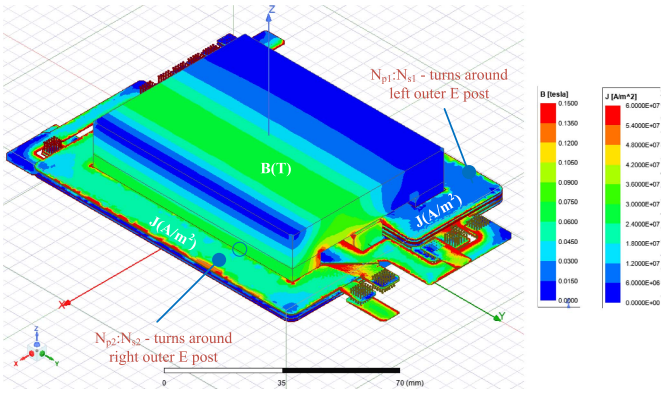

Fig. 17. Complete 3-D FE simulation using Ansys Maxwell software illustrating the flux density profile anticipated from the interaction between magnetizing and leakage flux and current density profile originating from loss of interleaving and effect of fringing fluxes from airgap. The excitation is $\hat{I}_p = 22\angle 0^\circ$ and $\hat{I}_s = 45.14\angle -0.5^\circ$. This simulation model is also used to extract the equivalent leakage inductance of the optimized structure as well before manufacturing a prototype.

constructed thereafter. The results obtained using this prototype are discussed in the following section.

V. Experimental Results

Fig. 18 shows the prototype integrated magnetic component constructed according to the design developed in the previous section. The relatively small customization required in the E core geometry was done using DMEGC DMR 51-W material and the windings were implemented in a PCB. PCB windings make such distributed transformer design quite easier since interconnection between the two elemental transformers can be made in the PCB itself. The PCB was constructed with 8 layers, using 4 oz copper thickness. The 8 primary turns required to sustain the volt–seconds on the converter prototype were

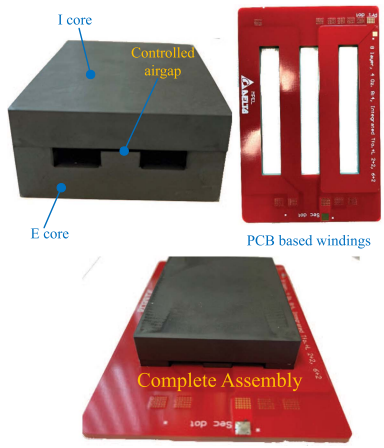

Fig. 18. Assembly of the proposed magnetic component integrating a controllable leakage inductance with the transformer. Minor customization in E core was done using DMEGC DMR 51-W material and the distributed windings are implemented on a PCB. The complete assembly is also shown using the core and PCB.

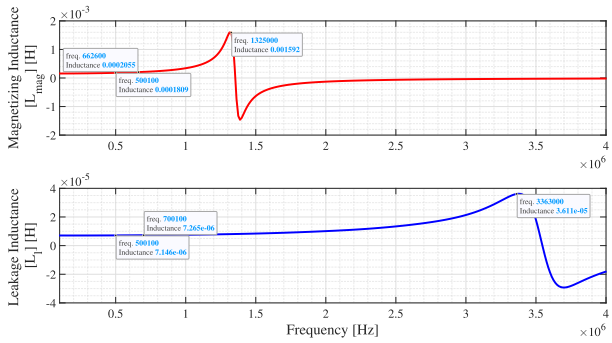

Fig. 19. Measurements of the assembled prototype shown in Fig. 18 using a HP4194 A network analyzer. To measure magnetizing inductance, the secondary windings are opened and impedance across the primary winding is measured and, similarly for the leakage inductance, secondary windings are shorted and lumped leakage inductance from the primary side is measured.

distributed as $N_{p1} = 2$, $N_{p2} = 6$ and the 4 secondary turns of the 2:1 transformer were distributed as $N_{s1} = 2$, $N_{s2} = 2$. Inductor L_1 was constructed using standard separate inductor technology, with 3 EILP 43 cores in parallel and 4 turns of Litz wire. Six AWG 46 Litz wires with 550 strands were paralleled for each turn. All other components in the application DC–DC converter of Fig. 9 were kept the same as mentioned in [27].

First, the constructed integrated magnetic component was characterized using an HP4194 A network analyzer. The measurement results are shown in Fig. 19, clearly indicating the magnetic structure achieves an equivalent leakage inductance of 7.3 μH across a wide frequency range from the primary side. Since no airgap was inserted between the outer posts of the E core segment, the magnetizing inductance is significantly larger ($L_{\text{mag}} \approx 205\,\mu$H) than the leakage inductance. As the windings are on PCB, a larger overlap between primary and secondary windings results in increased inter-winding capacitance of the transformer. Fig. 20 shows the integrated magnetic component assembled with the complete DC–DC converter prototype. With

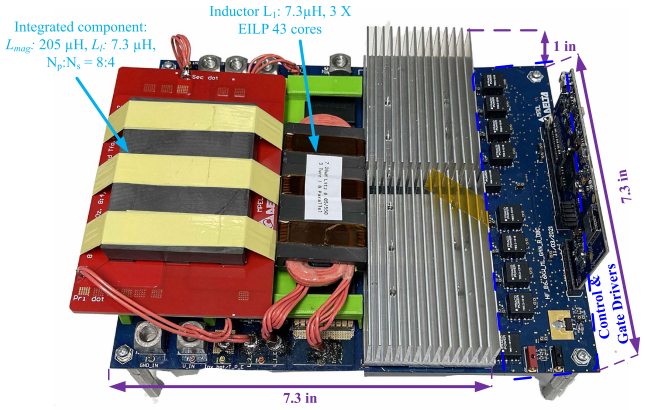

Fig. 20. Assembly of the complete converter shown in Fig. 9 using the previously constructed integrated magnetic component. The complete dimensions of the converter prototype is also marked, where, excluding the control and gate driver portion, the power stage achieves 7.4-kW/L power density.

TABLE I
INTEGRATED MAGNETIC COMPONENT DESIGN DETAILS

Core geometry and airgap	$a = 12$ mm; $b = 84$ mm; $c = 6$ mm; $w = 14$ mm; $l_g = 0.84$ mm;
Winding details	$N_p : N_s = 8 : 4$; $N_{p2} = 6$, $N_{s2} = 2$
PCB Stackup total thickness: 3.4 mm	8 layers, 40z Left side post of E core: Layers 1–4 and 7–8: Primary turns (N_{p2}), Layers 5–6: secondary turns (N_{s2}) Right side post of E core: Layers 7–8: primary turns (N_{p1}), Layers 3–4: secondary turns (N_{s1})
Core material	DMEGC DMR 51W
Measured Inductances	$L_{\text{mag}} = 205\,\mu\text{H}$; $L_l = 7.3\,\mu\text{H}$

this packaging, the overall converter achieves a power density of 7.3 kW/L. The construction details along with measured electrical parameters of the magnetic components are summarized in Table I.

Experimentally measured waveforms are presented at the envelope of the battery charging profile shown in Fig. 10. Fig. 21 shows the measured waveforms of inverter side switch node voltage (v_{inv}), inductor current (i_{L1}), rectifier switch node voltage (v_{rec}), inductor current (i_{L2}), transformer secondary current (i'_{L2}) and dc-link capacitor voltages for full bridge (FB) rectifier operation with $V_{\text{BATT}} \leq 500$ V. Fig. 21(a) shows operation at 270-V battery voltage with 20-A current at the constant current (CC) mode, and Fig. 21(b) and 21(c) shows operation in the CP mode with $V_{\text{BATT}} = 330$ and 390 V, respectively. In Fig. 22(a), (b), and (c), all the experimentally measured waveforms are presented for stacked half-bridge rectifier operation for three different output voltages of $V_{\text{BATT}} = 570$ V, $V_{\text{BATT}} = 670$ V, and $V_{\text{BATT}} = 800$ V, respectively, operating in the CP mode. As the rectifier is reconfigured, compared to the FB rectifier mode, the rectifier switching node voltage now becomes unipolar. As explained in [27], the converter is more stressed as the output voltage increases and the output current drops in the constant power mode of operation. The proposed integrated magnetic

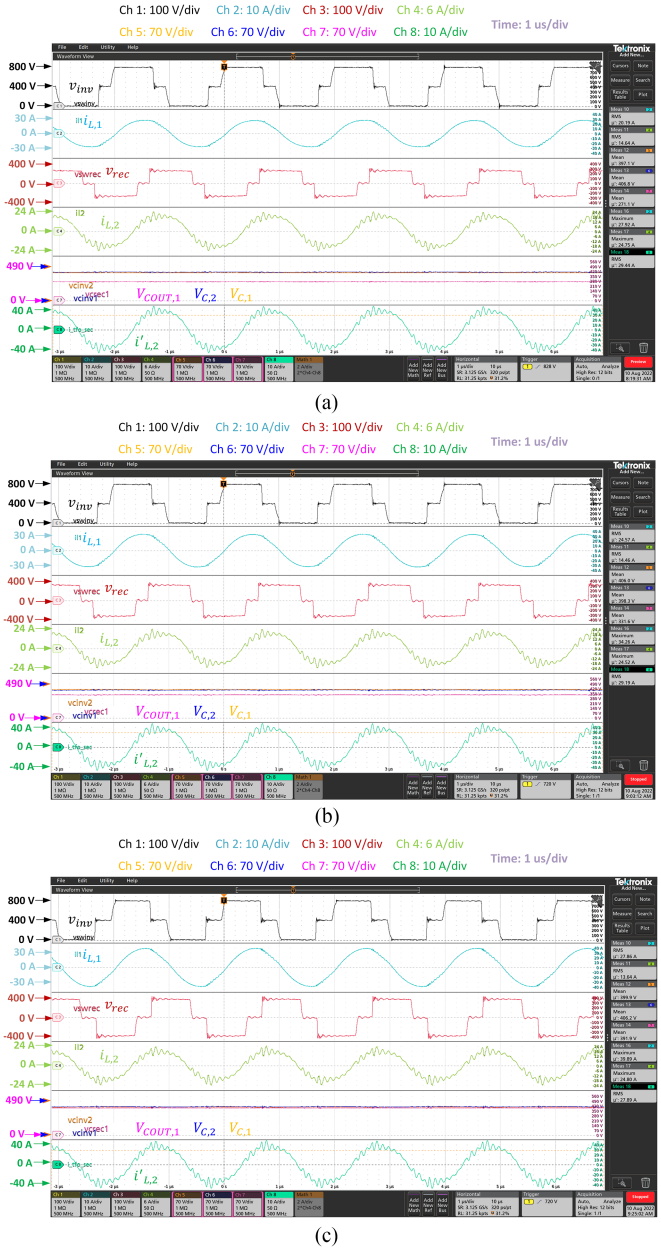

Fig. 21. Key measured waveforms for low-voltage battery operation using the FB rectifier in CC and CP modes for (a) $V_{\text{BATT}} = 270$ V, $I_{\text{BATT}} = 20$ A, (b) $V_{\text{BATT}} = 330$ V, $I_{\text{BATT}} = 20$ A, and (c) $V_{\text{BATT}} = 390$ V, $I_{\text{BATT}} = 17$ A.

component is capable of operating across the entire intended range of operations. The additional ringing observed in the currents $i_{L,2}$ and $i'_{L,2}$ is contributed by the larger interwinding capacitance of the integrated magnetic component. To illustrate the thermal stability of the converter, temperature measurements were made at the worst case operating point of $V_{\text{BATT}} = 800$ V. These results are presented in Fig. 23. In Fig. 23(a), the temperature profile of the integrated magnetic component resembles the 3-D FE simulation results shown in Fig. 17. The windings on the top layer are stressed due to heavy current density and the temperature profile on the core exactly follows the uneven flux density distribution on the core due to the interaction of

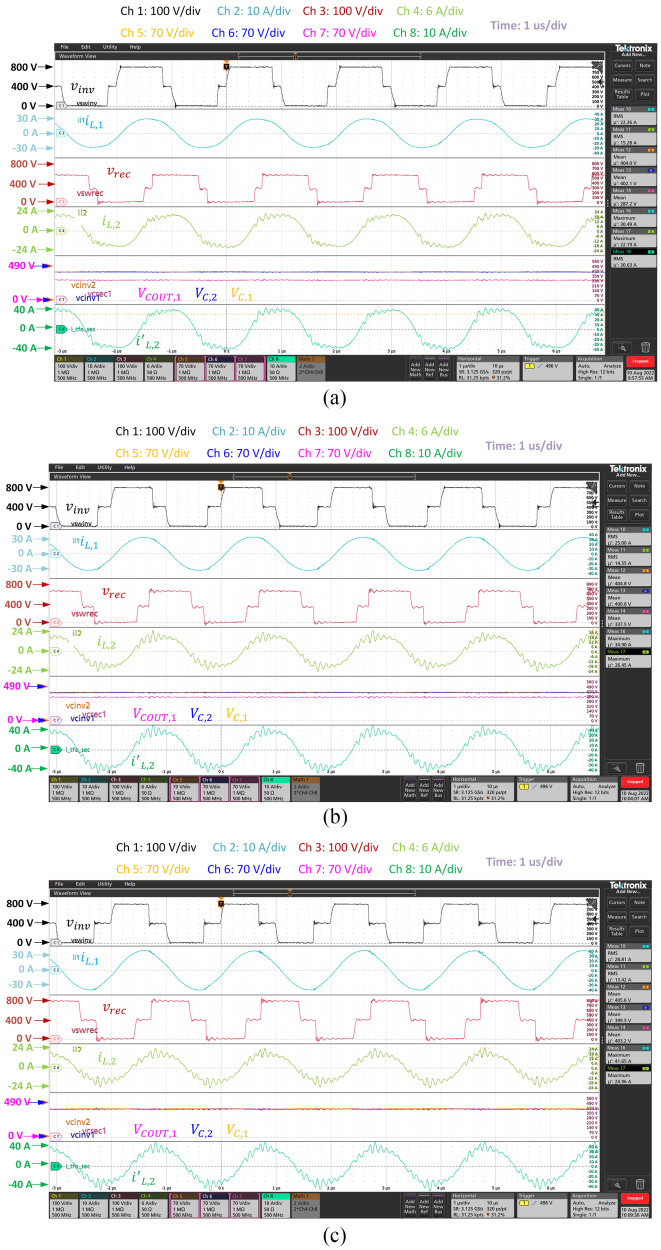

Fig. 22. Key measured waveforms for high-voltage battery operation using stacked half bridge (SHB) rectifier in CP mode for (a) $V_{\text{BATT}} = 570$ V, $I_{\text{BATT}} = 11.6$ A, (b) $V_{\text{BATT}} = 665$ V, $I_{\text{BATT}} = 9.9$ A, and (c) $V_{\text{BATT}} = 800$ V, $I_{\text{BATT}} = 8.25$ A.

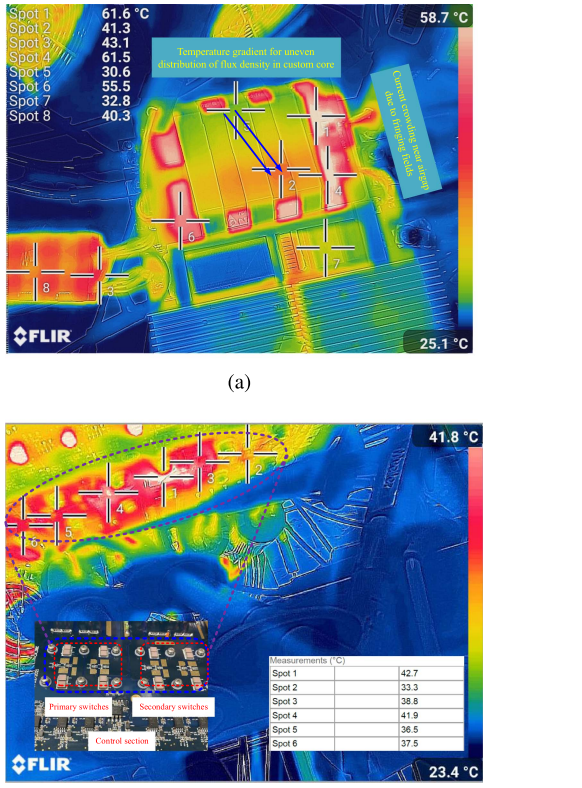

Fig. 23. Measured thermal images of the power converter operating at $V_{\text{BATT}} = 800$ V and $I_{\text{BATT}} = 8.25$ A. (a) Top view of the prototype demonstrating temperature rise on the magnetic component. The temperature profile on the core clearly shows the uneven flux density on different parts of the core. (b) Bottom view showcasing the temperature rise of the transistors.

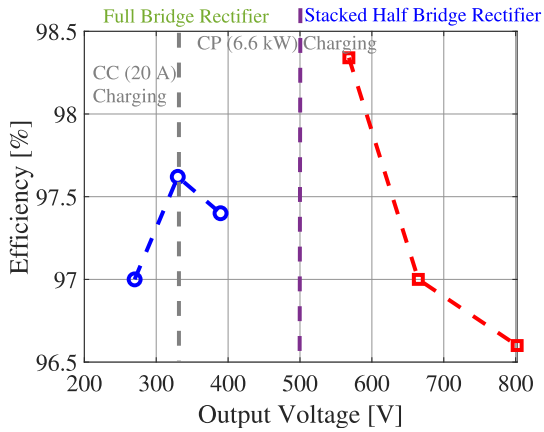

Fig. 24. Measured efficiency of the converter across entire output voltage range in CC and CP modes.

magnetizing and leakage flux. However, all temperatures are within permissible limits for EV charging applications using forced air cooling. Fig. 23(b) shows the temperature rise in the active components probed using electrical vias placed right underneath the devices. They also reach a maximum of 48 °C showing the thermal robustness of the converter. Finally, Fig. 24 shows the experimentally measured efficiency of the prototype converter across the entire output voltage range, operating at the envelop of the load profile shown in Fig. 10. The optimization of the transformer turns distribution presented in Section IV-B is done considering the power stage quantities (volt–seconds and winding currents of the transformer), when the converter is operated at $V_{\text{BATT}} = 570$ V. Hence, the peak efficiency of 98.4% is achieved at that point.

It should be noted that at this operating point, the experimentally measured loss shows excellent agreement with the model predicted loss shown in Fig. 15, with around 50-W

TABLE II
COMPARISON OF THE PROPOSED INTEGRATED MAGNETICS-BASED DC–DC CONVERTER WITH TWO BENCHMARK CASES

	Topology	Charging Profile	Magnetic Integration	Switching frequency	Power Density	Gain Range	Efficiency at Full Load
[9]	CLLC	CC CP CV	Yes, but not optimized	500 kHz	8 kW/L	1×	97.3-97.8%
[27]	Multi-level LCL-T	CC CP CV	Separate magnetics	500 kHz	7.3 kW/L	6×	97-98.2%
This Work	**Multi-level LCL-T**	**CC CP CV**	**Optimized integrated magnetics**	**500 kHz**	**7.3 kW/L**	**4×**	**96.5-98.4%**

The presented work's performance metrics is highlighted in bold face.

magnetics loss and 57-W semiconductor loss, further validating the high-frequency loss modeling approaches used in this work. The behavior of the integrated magnetic component is complex across wide operating ranges. As the output voltage increases, the magnetizing flux goes up (due to increased volt–seconds); however, the leakage flux drops as the current processed by the transformer windings reduce. This results in a drop in efficiency at other operating points of the converter. However, the converter is capable of maintaining greater than 96.5% efficiency across $4\times$ variation of the output voltage while being thermally stable. A comparison of the integrated magnetic component design and case study presented in this article with a state-of-the-art integrated magnetics approach and with an approach deploying separate magnetic components for similar converter level specifications is summarized in Table II. It should be noted how the presented work in this article achieves magnetic integration while working across a wider gain range while also preserving its superior efficiency and power density performance.

VI. SUMMARY AND CONCLUSION

This article presents the complete analysis of a technique to integrate and optimize a programmable resonant inductor as leakage inductance of a high-frequency transformer. The key contributions of the article can be summarized as follows.

1) Building upon an existing concept of leakage inductance integration using planar "E+I" cores, a generalized solution is given for asymmetrically distributed windings around the two outer posts of the "E" core segment. This previously unexplored solution provides important insights into how the same leakage inductance can be achieved with different distributions of primary and secondary turns among the elemental transformers, giving rise to a potential for loss optimization. The results are validated using simulations and measurements performed on the experimental prototype
2) The generalized reluctance model developed is further used to enhance the understanding of the interaction of magnetizing flux and leakage flux in the integrated component. This interaction prompts a specific modification in the core geometry and requires careful constructional optimization to maintain area and volume constraints. It is further validated in the hardware prototype using thermal images of the magnetic component how the flux profile in the core changes due to the interaction.
3) A novel optimization method is presented for the proposed magnetic structure, where, by redistributing the number of turns, the total loss can be minimized while keeping the required inductances the same. A step-by-step guideline to arrive at the optimized design from the given specifications is also highlighted.

The proposed magnetic component using the optimized design methodology is then applied to integrate a $7.8\,\mu$H series inductor with an 8:4 transformer for a 6.6-kW, 500-kHz LCL-T resonant DC–DC converter for EV charging application utilizing GaN transistors. On the prototype converter, using the integrated magnetic component, a peak efficiency of 98.4% was obtained using PCB windings.

REFERENCES

[1] P. L. Dowell, "Effects of eddy currents in transformer windings," in *Proc. Inst. Elect. Engineers*, vol. 113, no. 8, pp. 1387–1394, Aug. 1966.
[2] A. Rand, "Inductor size vs. Q: A dimensional analysis," *IEEE Trans. Compon. Parts*, vol. TCP-10, no. 1, pp. 31–35, Mar. 1963.
[3] W. Odendaal and J. Ferreira, "Effects of scaling high-frequency transformer parameters," *IEEE Trans. Ind. Appl.*, vol. 35, no. 4, pp. 932–940, Jul./Aug. 1999.
[4] J. Li, T. Abdallah, and C. R. Sullivan, "Improved calculation of core loss with nonsinusoidal waveforms," in *Proc. IEEE 36th Ind. Appl. Conf.*, vol. 4, 2001, pp. 2203–2210.
[5] T. Nakamura, "Snoek's limit in high-frequency permeability of polycrystalline NI-ZN, MG-ZN, and NI-ZN-CU spinel ferrites," *J. Appl. Phys.*, vol. 88, no. 1, pp. 348–353, 2000, doi: 10.1063/1.373666.
[6] W. Odendaal and J. Ferreira, "A thermal model for high frequency magnetic components," in *Proc. IEEE Conf. Rec. Ind. Appl. Conf. 32nd IAS Annu. Meeting*, vol. 2, 1997, pp. 1115–1122.
[7] W.-J. Gu and R. Liu, "A study of volume and weight vs. frequency for high-frequency transformers," in *Proc. IEEE Power Electron. Specialist Conf.*, 1993, pp. 1123–1129.
[8] D. J. Perreault et al., "Opportunities and challenges in very high frequency power conversion," in *Proc. IEEE 24th Annu. Appl. Power Electron. Conf. Expo.*, 2009, pp. 1–14.
[9] B. Li, Q. Li, and F. C. Lee, "High-frequency PCB winding transformer with integrated inductors for a bi-directional resonant converter," *IEEE Trans. Power Electron.*, vol. 34, no. 7, pp. 6123–6135, Jul. 2019.
[10] E. deJong, B. Ferreira, and P. Bauer, "Toward the next level of PCB usage in power electronic converters," *IEEE Trans. Power Electron.*, vol. 23, no. 6, pp. 3151–3163, Nov. 2008.
[11] Z. Ouyang and M. A. E. Andersen, "Overview of planar magnetic technology-fundamental properties," *IEEE Trans. Power Electron.*, vol. 29, no. 9, pp. 4888–4900, Sep. 2014.
[12] Z. Ouyang, O. C. Thomsen, and M. A. E. Andersen, "Optimal design and tradeoff analysis of planar transformer in high-power DC-DC converters," *IEEE Trans. Ind. Electron.*, vol. 59, no. 7, pp. 2800–2810, Jul. 2012.
[13] C. Fei, F. C. Lee, and Q. Li, "High-efficiency high-power-density LLC converter with an integrated planar matrix transformer for high-output current applications," *IEEE Trans. Ind. Electron.*, vol. 64, no. 11, pp. 9072–9082, Nov. 2017.
[14] M. Mu and F. C. Lee, "Design and optimization of a 380-12 V high-frequency, high-current LLC converter with GaN devices and planar matrix transformers," *IEEE Trans. Emerg. Sel. Topics Power Electron.*, vol. 4, no. 3, pp. 854–862, Sep. 2016.
[15] M. D'Antonio, S. Chakraborty, and A. Khaligh, "Planar transformer with asymmetric integrated leakage inductance using horizontal air gap," *IEEE Trans. Power Electron.*, vol. 36, no. 12, pp. 14014–14028, Dec. 2021.
[16] J. Biela and J. Kolar, "Electromagnetic integration of high power resonant circuits comprising high leakage inductance transformers," in *Proc. IEEE 35th Annu. Power Electron. Specialists Conf.*, vol. 6, 2004,pp. 4537–4545.
[17] M. Mu, L. Xue, D. Boroyevich, B. Hughes, and P. Mattavelli, "Design of integrated transformer and inductor for high frequency dual active bridge GaN charger for PHEV," in *Proc. IEEE Appl. Power Electron. Conf. Expo.*, 2015, pp. 579–585.
[18] Y. Liu, H. Wu, J. Zou, Y. Tai, and Z. Ge, "CLL resonant converter with secondary side resonant inductor and integrated magnetics," *IEEE Trans. Power Electron.*, vol. 36, no. 10, pp. 11316–11325, Oct. 2021.

[19] M. H. Ahmed, A. Nabih, F. C. Lee, and Q. Li, "Low-loss integrated inductor and transformer structure and application in regulated LLC converter for 48-V bus converter," *IEEE Trans. Emerg. Sel. Topics Power Electron.*, vol. 8, no. 1, pp. 589–600, Mar. 2020.

[20] Y. Park, S. Chakraborty, and A. Khaligh, "DAB converter for EV onboard chargers using bare-die SiC MOSFETs and leakage-integrated planar transformer," *IEEE Trans. Transport. Electrific.*, vol. 8, no. 1, pp. 209–224, Mar. 2022.

[21] J. Zhang, Z. Ouyang, M. C. Duffy, M. A. E. Andersen, and W. G. Hurley, "Leakage inductance calculation for planar transformers with a magnetic shunt," *IEEE Trans. Ind. Appl.*, vol. 50, no. 6, pp. 4107–4112, Nov./Dec. 2014.

[22] Y. Liu, X. Huang, Y. Dou, Z. Ouyang, and M. A. E. Andersen, "GaN-based ZVS bridgeless dual-SEPIC PFC rectifier with integrated inductors," *IEEE Trans. Power Electron.*, vol. 36, no. 10, pp. 11483–11498, Oct. 2021.

[23] J. H. Spreen, "Electrical terminal representation of conductor loss in transformers," *IEEE Trans. Power Electron.*, vol. 5, no. 4, pp. 424–429, Oct. 1990.

[24] R. W. Erickson and D. Maksimović, "Basic Magnetics Theory. Cham, Switzerland:Springer, 2020, pp. 409–458, doi: 10.1007/978-3-030-43881-4_10.

[25] J.-P. Vandelac and P. Ziogas, "A novel approach for minimizing high-frequency transformer copper losses," *IEEE Trans. Power Electron.*, vol. 3, no. 3, pp. 266–277, Jul. 1988.

[26] S. Mukherjee, Y. Gao, and D. Maksimović, "Reduction of AC winding losses due to fringing-field effects in high-frequency inductors with orthogonal air gaps," *IEEE Trans. Power Electron.*, vol. 36, no. 1, pp. 815–828, Jan. 2021.

[27] S. Mukherjee, J. M. Ruiz, and P. Barbosa, "A high power density wide range DC-DC converter for universal electric vehicle charging," *IEEE Trans. Power Electron.*, vol. 38, no. 2, pp. 1998–2012, Feb. 2023.

[28] M. Borage, K. V. Nagesh, M. S. Bhatia, and S. Tiwari, "Resonant immittance converter topologies," *IEEE Trans. Ind. Electron.*, vol. 58, no. 3, pp. 971–978, Mar. 2011.

[29] S. Mukherjee, V. Yousefzadeh, A. Sepahvand, M. Doshi, and D. Maksimović, "High-frequency wide-range resonant converter operating as an automotive LED driver," *IEEE Trans. Emerg. Sel. Topics Power Electron.*, vol. 9, no. 5, pp. 5781–5794, Oct. 2021.

Satyaki Mukherjee (Member, IEEE) received the integrated B.Tech. and M.Tech. degrees in electrical engineering from the Indian Institute of Technology Kharagpur, Kharagpur, India, in 2018, and the Ph.D. degree in electrical engineering with focus on power electronics from the Colorado Power Electronics Center (CoPEC), University of Colorado Boulder, Boulder, CO, USA, in May 2021.

He is currently a Member of R&D Staff with Milan Power Electronics Laboratory (MPEL), Delta Electronics (Americas), Ltd., Research Triangle Park. He was a Graduate Student Intern with the Kilby Labs of Texas Instruments Inc., Santa Clara, CA, USA, in 2019. His current research interests include power electronics for transportation electrification and renewable energy sources, high-frequency power conversion using wide bandgap semiconductors, high-frequency magnetics design, automotive lighting, and digital control of switched-mode power converters.

Peter Barbosa (Senior Member, IEEE) received the Ph.D. degree in electrical engineering from Virginia Polytechnic Institute and State University (Virginia Tech), Blacksburg, VA, USA, in 2002.

From 2001 to 2003, he was the Technical Director with the Center for Power Electronics Systems, Virginia Tech. In 2003, he was with ABB Corporate Research, Baden, Switzerland, as a Scientist, and later as the Manager of the Power Electronics and System Applications Group. At ABB, he developed innovative multilevel power converters for high-power applications by introducing novel hybrid multilevel power conversion concepts. Since 2008, he has been with Delta Electronics, first in Taiwan developing high-efficiency telecom power supplies and heading medium-voltage drive products, and recently the Director with Milan Jovanović Power Electronics Laboratory, Research Triangle Park, USA.